Journal of Materials Chemistry B

ROYAL SOCIETY OF CHEMISTRY

PAPER

View Article Online
View Journal | View Issue

Cite this: J. Mater. Chem. B, 2024, 12, 9375

Small intestine submucosa decorated 3D printed scaffold accelerated diabetic bone regeneration by ameliorating the microenvironment†

Jie Tan,‡[abc] Zecai Chen,‡[b] Zhen Xu,‡[b] Yafang Huang,[b] Lei Qin,[b] Yufeng Long,[b] Jiayi Wu,[b] Hantao Yang,[b] Xuandu Chen,[b] Weihong Yi,[b] Ruiqiang Hang,[d] Min Guan,[a] Huaiyu Wang,*[a] Ang Gao*[a] and Dazhi Yang*[b]

The 3D printed scaffolds constructed from polymers have shown significant potential in the field of bone defect regeneration. However, the efficacy of these scaffolds can be markedly reduced in certain pathological conditions like diabetes, where an altered inflammatory microenvironment and diminished small blood vessels complicate the integration of these polymers with the host tissue. In this study, the bioactivity of a 3D-printed poly(lactide-*co*-glycolide) (PLGA) scaffold is enhanced through the integration of hydroxyapatite (HA), icariin (ICA), and small intestine submucosa (SIS), a form of decellularized extracellular matrix (dECM). The decoration of SIS on the 3D-printed PLGA/HA/ICA scaffold not only improves the mechanical and degradative performance, but also extends the release of ICA from the scaffold. Both *in vitro* and *in vivo* studies demonstrate that this functionalized scaffold mitigates the persistent inflammatory conditions characteristic of diabetic bone defects through inducing macrophages towards the M2 phenotype. Additionally, the scaffold promotes angiogenesis by enhancing the migration and tube formation of vascular cells. Furthermore, the synergistic effects of ICA and SIS with the HA scaffolds contribute to the superior osteogenic induction capabilities. This functionalization approach holds significant promise in advancing the treatment of bone defects within the diabetic population, paving a step forward in the application of polymer-based 3D printing technologies in regenerative medicine.

Received 9th April 2024,
Accepted 19th August 2024

DOI: 10.1039/d4tb00772g

rsc.li/materials-b

1. Introduction

Bone defects are refractory diseases, particularly in cases who are suffering from diabetes.[1,2] The typical characteristics of diabetes include biochemical dysfunction, inflammatory microenvironment, abnormal sugar levels, and decreased antioxidant capacity, which set intractable obstacles to the physiological healing process of critical-sized bone defects.[3–6] These pathological disturbances further lead to a low metabolic state for bone formation and bone absorption, which can then be followed by the reduction of small blood vessels, pathological lesions of nerves, as well as decreased mobilization of bone marrow stem cells.[7–10] Furthermore, inflammatory M1 macrophages are dominant in this pathological condition, which secrete a series of inflammatory cytokines such as IL-1β and TNF-α to disrupt the physiological microenvironment of damaged tissues.[11–14] Therefore, for the repair of diabetic bone defects, the implants should be specifically designed and multiply functionalized when the pathological characteristics of diabetes are taken into overall consideration.

Owing to the unique advantages such as customized design, automated construction, and flexible selectivity of printing materials, 3D printing techniques have been widely utilized to fabricate scaffolds for the repair of bone defects.[15–18] Nowadays, a series of biomaterials have been developed for the 3D construction of bone scaffolds.[19–21] In this context, polymeric biomaterials, especially the polyesters with degradable properties, are more preferable than the biomedical metals/alloys and ceramics for 3D printing, which are due to their relatively low melting point and ease of fabrication.[22–24] Among the various

[a] Center for Human Tissues and Organs Degeneration, Shenzhen Institute of Advanced Technology, Chinese Academy of Sciences, Shenzhen, 518055, China. E-mail: hy.wang1@siat.ac.cn, ang.gao1@siat.ac.cn
[b] Department of Spine Surgery & Innovative Laboratory of Orthopedics, Huazhong University of Science and Technology Union Shenzhen Hospital, Shenzhen, 518052, China. E-mail: qpopop1977@163.com
[c] Orthopaedic department, Wuhan Fourth Hospital, Wuhan, 430030, China
[d] Shanxi Key Laboratory of Biomedical Metal Materials, Taiyuan University of Technology, Taiyuan, 030024, China

† Electronic supplementary information (ESI) available. See DOI: https://doi.org/10.1039/d4tb00772g

‡ These authors have contributed equally to this work.

types of biodegradable polyesters, poly(lactic-*co*-glycolic acid) (PLGA) is outstanding as its degradation properties can be readily adjusted by varying the ratio of polyglycolide and polylactide, whereas the degradation performances of other polyesters such as polycaprolactone (PCL) and polylactic acid (PLA) can only be tuned by altering their molecular weight.[25,26] Nonetheless, similar with the other biodegradable polyesters, PLGA provides good biocompatibility, but it is still lacking of the bioactivity indispensable for bone regeneration. It is also noteworthy that the degradation product of PLGA is acidic, which is detrimental to the healing process of defected bones. Therefore, when PLGA is solely used as the basic material for 3D printing, the fabricated scaffold is far from satisfactory for the repair of bone defects.[27] Incorporation of hydroxyapatite (the inorganic component of nature bone) with PLGA is a valid strategy to address these issues, as hydroxyapatite can not only neutralize the acidity after PLGA degradation, but also provide good bioactivity to facilitate bone regeneration.[28,29] However, this strategy cannot meet the strict requirements of bone repair under diabetic condition, as the other knotty problems such as immunoregulation and vascularization remain unsettled.

The diverse and multiple functions of naturally derived biomaterials give some hints to the design of bone scaffolds. In particular, small intestine submucosa (SIS), the extracellular matrix derived from decellularization of porcine small intestine, is a promising kind of naturally derived biomaterials.[30,31] Our previous studies have demonstrated that the bioactive components such as cytokines, collagens, and exosomes are well maintained in SIS, which can promote the M2 polarization of macrophages to facilitate the subsequent process of tissue repair.[32–34] On the other hand, icariin is a kind of compounds extracted from epimedium, which can reverse the development of osteoporosis and facilitate the regeneration of small blood vessels.[35,36] Hence, there is a great chance to fulfill the various functional requirements of diabetic bone repair by simultaneously introducing hydroxyapatite, SIS and icariin into the 3D-printed PLGA scaffold.

Here in this study, we incorporated PLGA with hydroxyapatite and icariin to construct the composites into scaffolds by 3D printing. Afterwards, SIS was decorated on the surface of 3D-printed scaffolds to achieve better performances by coating and crosslinking. Both *in vitro* and *in vivo* experiments showed that the functionalized 3D-printed scaffolds not only provided desirable immunoregulatory effect, but also facilitated angiogenesis and osteogenesis during the subsequent process. Overall, our study paves a new way for the construction of multifunctional scaffolds, which enables the satisfactory repair of bone defects under diabetic condition.

2. Materials and methods

2.1 Fabrication of SIS-decorated 3D-printed scaffold

To prepare the printing slurry, 3.2 g of PLGA, 0.8 g of hydroxyapatite (HA), and icariin with the final concentration of 10 μM were sequentially added to a 20 mL 1,4-dioxane solution according to group assignments. The scaffolds were printed into grid-like structures using a 3D-printing apparatus (Regenovo, China), employing a 27 G printing nozzle at the printing speed of 50 mm s^{-1} and pneumatic pressure of 0.1 MPa on the −15 °C receiver plate. Then the obtained scaffolds were freeze-dried to facilitate the removal of organic solvent 1,4-dioxane. The scaffolds consisting of PLGA and HA were designated as PH, and those integrating PLGA, HA, and icariin were denoted as PHI, where the final concentration of HA was 20%.

Following lyophilization, the 3D-printed scaffolds were sequentially washed with 100% ethanol and 1.0× PBS solute ion for three times. A 3% SIS solution was employed to coat the PHI scaffolds, which were then immersed and crosslinked in solutions of 2.5 mg mL^{-1} carbodiimide (EDC, Aladdin, China) and 0.63 mg mL^{-1} *N*-hydroxysuccinimide (NHS, Aladdin, China). These treated scaffolds were labelled as PHIS. The SIS solution was prepared according to our previously published study.[30] Subsequently, the PHIS scaffolds were washed with 1.0× PBS solution for three times to eliminate any residual crosslinking reagents. Finally, the scaffolds were lyophilized again and stored at −20 °C for further use.

2.2 Materials characterization

The geometry and architecture of 3D-printed scaffolds were observed by light microscope. After sputter-coating the samples with gold, their surface morphology was characterized using scanning electron microscope (SEM, EVO 10, ZEISS, Germany) at an accelerating voltage of 20.0 kV. Fourier transform infrared spectroscopy (FTIR, Thermo, USA) was utilized to analyze the changes in surface functional groups within a wavenumber range of 400–4000 cm^{-1}. X-Ray diffraction (XRD, Nalytical, Netherlands) with Co Kα radiation (λ = 1.78897 Å) in the 2θ range of 10–70° at step size: 0.02° s^{-1} was used to detect the structure of the 3D-printed scaffolds. Thermogravimetric and differential scanning calorimetry (TG-DSC, NETZSCH, Germany) with a range of room temperature to 1100 °C and a heating rate of 10 °C was applied to analyze the thermostability of the 3D-printed scaffolds. Inductively coupled plasma optical emission spectrometer (ICP-OES, PerkinElmer, USA) was used to detect the calcium and phosphorus release profiles (days 1, 3, 5, 7, 9, 11, 13, 15) of the 3D-printed scaffolds. The release profile of icariin from the PHI and PHIS groups was tested by high performance liquid chromatography (HPLC, Thermo, USA). The mechanical behaviors of those 3D-printed scaffolds were tested by a mechanical testing instrument (CARE, China), where the compressive properties of those scaffolds (diameter: 10 mm; height: 10 mm) were tested with a speed of 1 mm min^{-1}, and the stress–strain curves of those 3D-printed scaffolds were calculated and analyzed according to the recorded load and displacement parameters. The elemental concentration and distribution of Ca and P on the surface of 3D-printed scaffolds were determined by energy dispersive X-ray spectroscopy (EDS, ZEISS, Germany). The degradation rates of the 3D-printed scaffolds (5 × 10 × 10 mm^3; rotatory speed: 50 rpm in room temperature) at days 0, 5, 10, 15, 20, 25,

30, 35 and 40 were weighed and calculated, and the equation was calculated as follows:

$$\text{Degradation rate (\%)} = M_t/M_0 \times 100\%$$

where M_0 was the initial mass of the scaffolds, and M_t was the mass of scaffolds at predetermined time points.

2.3 Biocompatibility

Bone marrow-derived stem cells (BMSCs) were employed to evaluate the biocompatibility of those 3D-printed scaffolds. BMSCs were seeded on 3D-printed scaffolds in a 96-well plate at the density of 2×10^3 cells per well, and the culture media were refreshed every other day. After the cells were incubated for 1, 2, 3, and 5 days, cell proliferation was determined using a CCK-8 kit (Dojindo, Japan). At each time point, the culture medium was refreshed with serum-free medium containing 10% CCK-8. After incubation in dark at 37 °C for 2 hours, the media were collected and absorbance at the wavelength of 450 nm was measured by a microplate reader (Thermo Scientific, USA).

The cytotoxicity of the 3D-printed scaffolds was evaluated by live/dead assay kit containing calcein-AM and propidium iodide (PI) (Beyotime, China). After BMSCs were incubated on scaffolds as described above for 2 days, they were stained with calcein/PI solution according to the manufacture's protocols, and were then observed using a confocal laser scanning microscope (CLSM, Nikon, Japan).

2.4 The inflammatory response of macrophages

The inflammatory response of macrophages was assessed using murine-derived macrophage cell line RAW264.7. Cells were cultured for 2 days in scaffold extracts, which were prepared according to the ISO 10993-12:2021 protocols. After fixation by 4% paraformaldehyde, permeabilization with 0.1% Triton-X 100, and blockade by 10% goat serum, RAW264.7 cells were incubated with primary antibodies of mannose receptor (CD206, 1:200 dilution, ab300621, Abcam), inducible nitric oxide synthase (iNOS, 1:200 dilution, ab178945, Abcam), and F4/80 (1:200 dilution, ab6640, Abcam) at 4 °C in dark overnight. Then cells were incubated with secondary antibodies of Alexa Fluor 594 goat anti-rat (1:1000 diluted, 8889s, CST) and Alexa Fluor 488 goat anti-rabbit (1:1000 diluted, 4416s, CST) in dark for another 1 h at room temperature. After counterstaining with DAPI and sealing with anti-fluorescent quenching coverslips, the immunofluorescence of RAW264.7 cells was observed using CLSM and analyzed by ImageJ 1.8.0 software.

The expression of immune-related genes in RAW264.7 was evaluated by quantitative polymerase chain reaction (qPCR). After cells were cultured for 2 days, total RNA was extracted and reversely transcribed into complementary DNA (cDNA). Then qPCR was performed on a real-time thermocycler (LC 96,

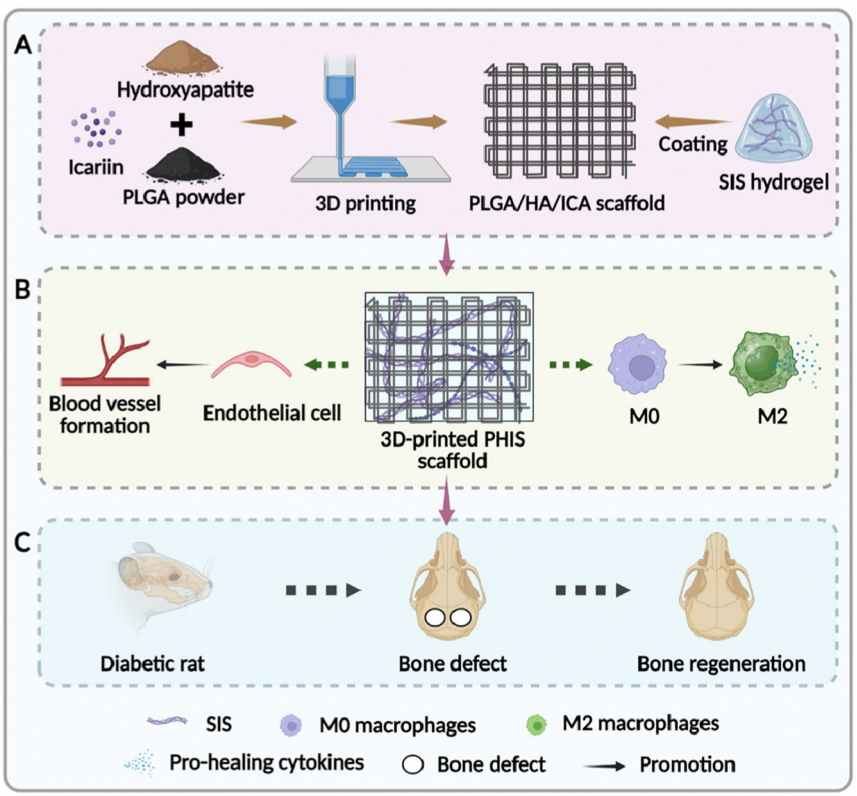

Fig. 1 The graphical illustration of this study. (A) Fabrication of the 3D-printed scaffold with PLGA, nano-hydroxyapatite, and icariin, which is then coated and crosslinked with SIS; (B) biological evaluation of the 3D-printed scaffold *in vitro*, where M2 macrophage polarization and enhanced angiogenesis are observed; (C) successful bone regeneration of diabetic rats is attained by the 3D-printed scaffold *in vivo*.

Roche, Switzerland) using a mixture of TB Green® Premix Ex Taq™ II mix (Takara, Japan) and primers as listed in Table S1 (ESI†). The amplification steps were 95 °C for 30 s, followed by 40 cycles of 95 °C for 10 s and 60 °C for 30 s. Relative gene expressions were calculated by the $2^{-\triangle\triangle Ct}$ method with β-actin serving as the housekeeping gene for normalization.

2.5 *In vitro* angiogenic study

The angiogenic effects of scaffold extracts was evaluated using human umbilical vein endothelial cells (HUVECs) through scratch assay and tube formation assay. For scratch assay, HUVECs were seeded into a 6-well plate at the density of 1.2×10^6 per well and starved for 24 h. Then a scratch was created using the tip of a 200 μL pipette, followed by rinsing to remove the unadhered cells and cell debris. The culture medium was subsequently replaced with extracts derived from the 3D-printed scaffolds. HUVECs were observed under a light microscope at the timepoints of 0, 24, and 48 hours after scratch. The acquired images were analyzed by the ImageJ 1.8.0 software, and the migration rate was calculated as follows:

$$\text{Migration rate (\%)} = (S_0 - S_t)/S_0 \times 100\%$$

where S_0 was the initial area of the scratch, and S_t was the area at each timepoint.

Matrigel (Sigma, USA) was used for tube-formation assay. 200 μL of Matrigel was added to each well of 24-well plate and incubated at 37 °C for gelation. Then HUVECs were seeded into each well at a density of 2.0×10^4 per well, using the extracts of the 3D-printed scaffolds as the medium. After being cultured for 0, 2, and 8 h, the formed tubes were observed and photographed under a light microscope. For quantitative analysis of the tubular structures, ImageJ 1.8.0 software equipped with an Angiogenesis Analyzer package was employed to analyze the length of tubes and the numbers of branches, junctions, and nodes. The mRNA gene expressions associated with angiogenesis were also tested by qPCR with the same protocols as that in Section 2.4, and the primers were listed in Table S2 (ESI†).

2.6 *In vitro* osteogenic study

After MC3T3-E1 cells were cultured in the extracts derived from the 3D-printed scaffolds for 7 days, cells were fixed by 4% paraformaldehyde for 30 min before being stained with alkaline phosphatase (ALP) Color Development Kit (Beyotime, China). In addition, expression of osteogenesis-related genes in MC3T3-E1 cells were evaluated following the protocols described in Section 2.4 and the primers were listed in Table S3 (ESI†). The degree of extracellular matrix mineralization after culture of 21 days was determined by Alizarin Red S

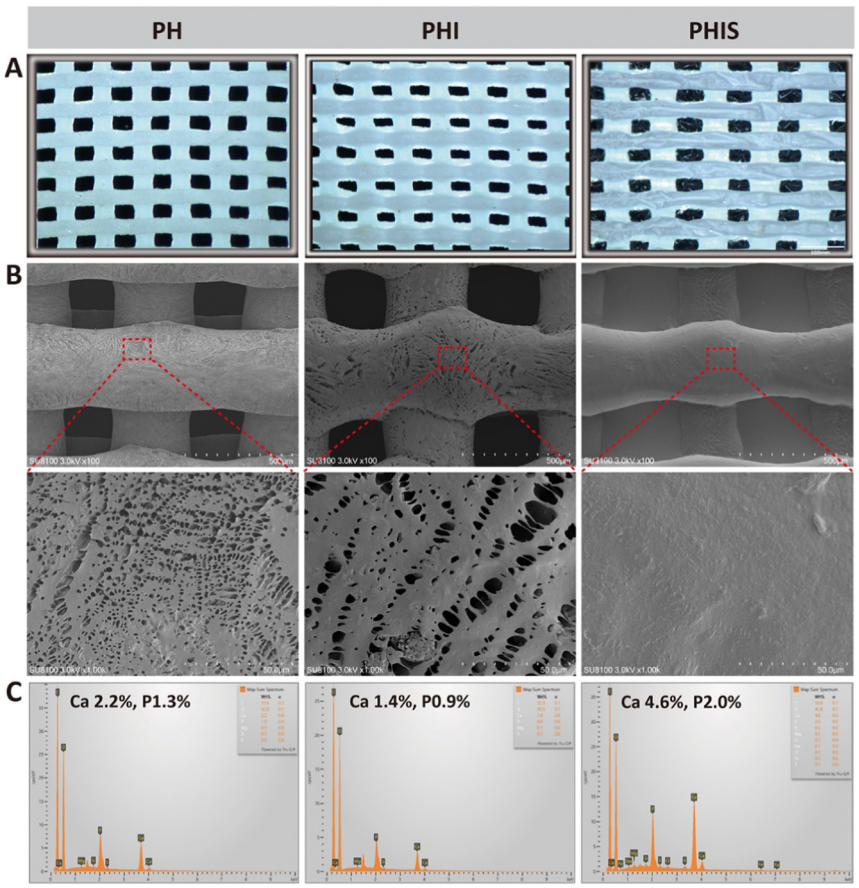

Fig. 2 The characterization of the 3D-printed scaffolds. (A) Morphological view under light microscope; (B) SEM images; (C) elemental composition by EDS.

(ARS, Beyotime, China) staining, and the obtained images were analyzed by ImageJ 1.8.0.

2.7 Establishment of diabetic rat model and surgical procedures

All the animal experiments and protocols were approved by the institutional animal care and use committee (IACUC) of Shenzhen TopBiotech Co., Ltd. (IACUC no. 2023-0302). Male Sprague Dawley (SD) rats, weighting approximately 200 g and acquired from Guangdong Experiment Animal Center, were used in this *in vivo* study. To induce diabetes, the rats were fasted for 24 h and then received an intraperitoneal injection of 75 mg kg^{-1} streptozotocin (STZ, MCE, USA). Three days after injection, blood sugar levels were measured, and rats with levels below 11.1 mM received another dose of 20 mg kg^{-1} STZ.

Two weeks after induction of diabetes, the rats were anesthetized using isoflurane. Following skin preparation and disinfection, a 1.5 cm midsagittal incision was made to expose the skull. Then a critical-sized bone defect was created using a 5 mm dental trephine bur, followed by implantation of the 3D-printed scaffolds (diameter: 5 mm, weight: 100 mg) into the defects. The surgical incisions were subsequently closed using interrupted sutures. In addition, these 3D-printed scaffolds were also subcutaneously implanted into the dorsal region of the rats. Post-operative care included administration of 30 mg kg^{-1} ampicillin for infection prevention and 2 mg kg^{-1} meloxicam pain relief. At 4 and 8 weeks after surgical operation, the skulls of the diabetic rats were collected from the sacrificed rats and fixed in 4% polyformaldehyde for further analysis.

2.8 Micro-CT scan

The newly formed bone in defects was detected and imaged using Micro-CT (NEMO, China) under 80 kV voltage, 100 μA current, and 18 μm voxel size. Acquired slices were reconstructed into 3D images using accompanied reconstruction software with the grayscale set at 220. The regenerated new bone volume, bone volume/total volume (BV/TV), and bone mineral density (BMD) of the diabetic rat skulls were determined by 3D bone morphometric analysis.

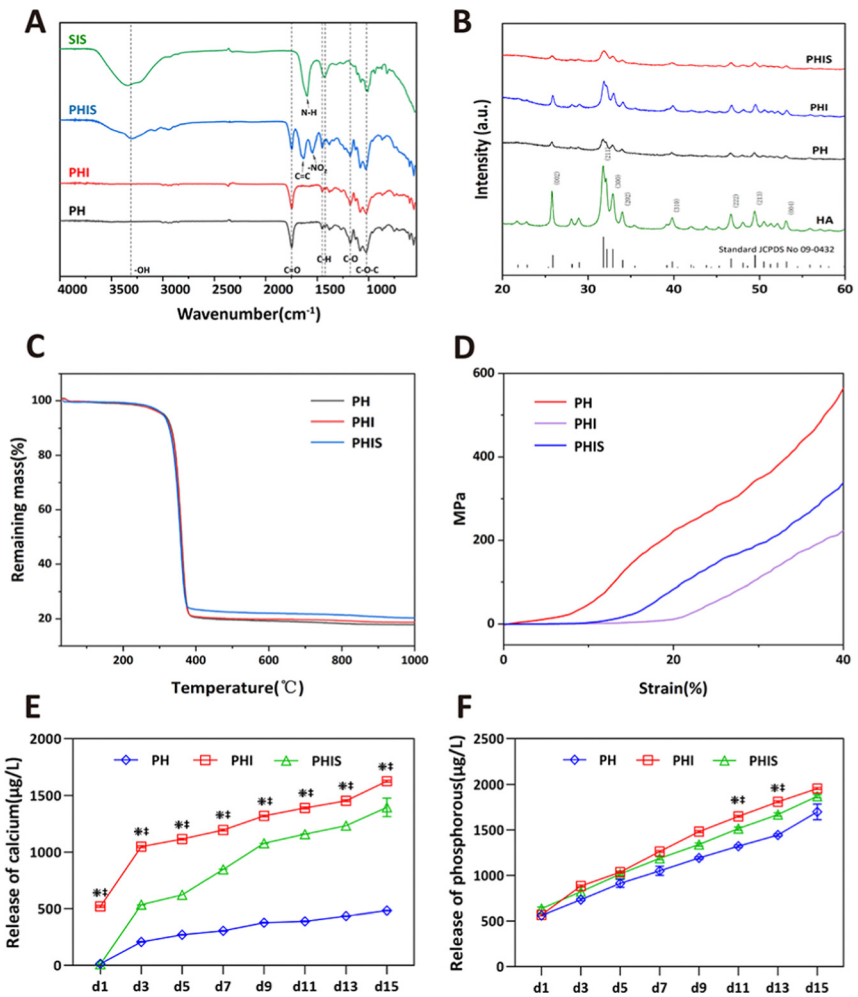

Fig. 3 The physicochemical characterization of the 3D-printed scaffolds. (A) FTIR spectra, (B) XRD patterns, (C) TGA thermograms, and (D) Mechanical performances of those 3D-printed scaffolds; (E) and (F) calcium and phosphorus ions released from those 3D printed scaffold at different timepoints. *$p < 0.05$, *vs.* PHI; ‡$p < 0.05$, *vs.* PH.

2.9 HE and Masson's trichrome staining

After micro-CT scanning, the rat skull samples were decalcified by 10% ethylene diamine tetracetic acid (EDTA) (Solarbio, China) for 1 month in a 37 °C shaker, with the EDTA solution being weekly refreshed. Subsequently, the samples were dehydrated by a graded series of ethanol, embedded in paraffin, and sliced with rotary microtome (Leica, German). Following sectioning, the slices were rehydrated and stained with Hematoxylin–Eosin (HE) and Masson's trichrome staining (Beyotime, China), respectively.

2.10 Immunohistochemistry and immunofluorescence

Paraffin-embedded slices of rat skin and skull samples were sequentially dewaxed, rehydrated, and water-bathed in sodium citrate solution (ZSGB-BIO, China) (pH = 6.2) for antigen retrieval (60 °C, overnight). The slices were then blocked using a 10% goat serum solution and treated with 3% H_2O_2 to quench endogenous hydrogen peroxidases. Primary antibodies targeting CD206 (1:500 dilution, ab300621, Abcam), CD31 (1:500 dilution, ab281583, Abcam), and ALP (1:500 dilution, ab300621, Abcam) were respectively incubated with the slices in dark overnight. Subsequently, the sections were exposed to corresponding secondary antibodies and DAB kit (Boster, China). The expression changes were observed and photographed under a microscope.

2.11 Statistical analysis

SPSS software (version 22.0, IBM, USA) was utilized to analyze the data in this study. Results were presented as mean ± standard deviation. One-way analysis of variance (ANOVA)

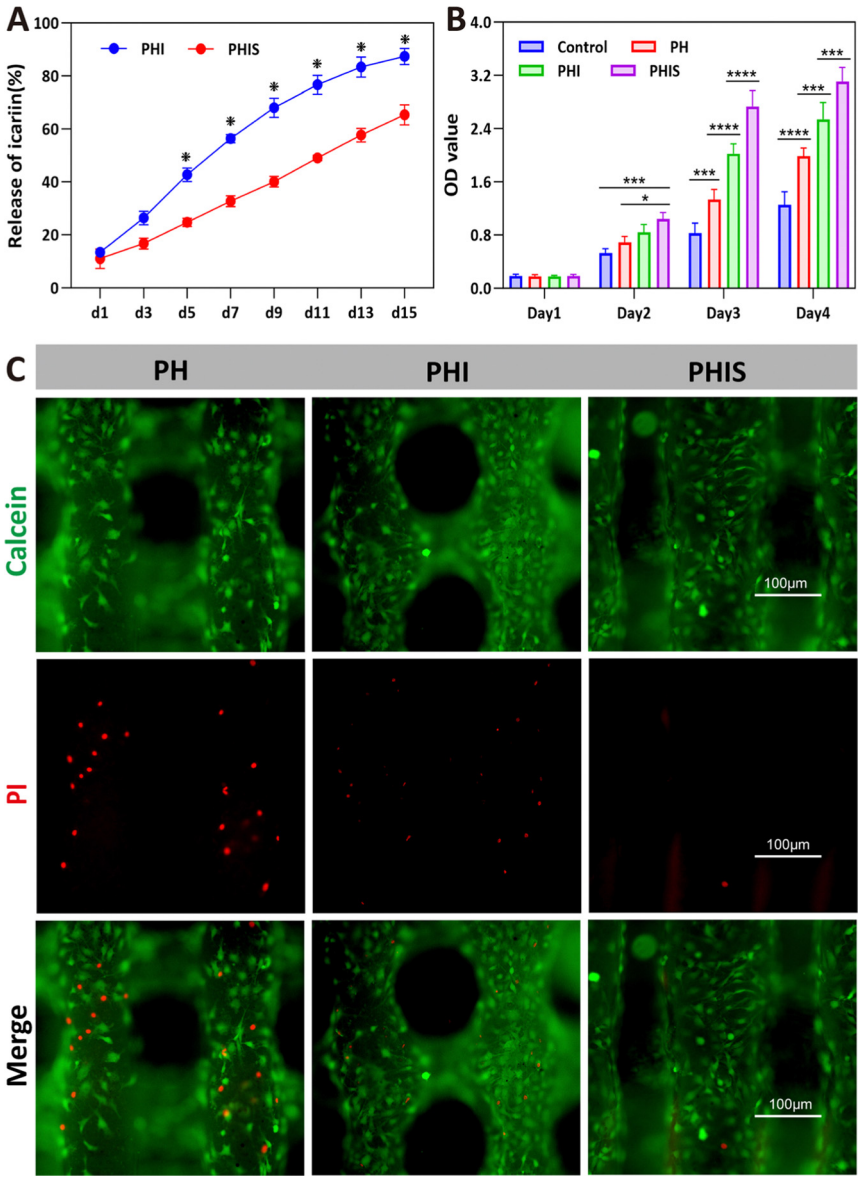

Fig. 4 Biocompatibility assessment of the 3D-printed scaffolds. (A) Icariin release profile of those 3D-printed scaffolds; (B) cell proliferation by CCK-8 assay; (C) calcein/PI staining of BMSCs on those 3D-printed scaffolds. *$p < 0.05$, **$p < 0.01$, ***$p < 0.001$, ****$p < 0.0001$.

followed by *post hoc* Tukey's test was performed to determine the statistical significance between groups. A difference at p value <0.05 was considered to be significant.

3. Results and discussion

3.1 Characterization of the 3D-printed scaffolds

3D-printing technology has been widely used in bone tissue engineering for its ability to provide 3D structures, which not only facilitate nutrient exchange and cell infiltration but also offer flexibility in customization.[29,37] Additionally, this technology simplifies the incorporation of bioactive compounds into the scaffolds.[16,17] As shown in Fig. 1, in this study, hydroxyapatite (HA) and icariin are integrated into the 3D-printed PLGA to enhance the osteogenic induction capacity of the scaffolds, while the small intestine submucosa (SIS) is decorated on the surface to render the scaffold with immunomodulatory and pro-angiogenic properties. The samples are designated as PH (PLGA scaffold consisting HA), PHI (PLGA scaffold consisting HA and icariin), and PHIS (PLGA scaffold consisting HA and icariin, with SIS decorated on the surface).

Microscopic observation of the 3D-printed scaffolds reveals a palisade-like structure with notably expanded grids in PHIS group (Fig. 2(A)). According to the SEM observation shown in Fig. 2(B), interconnected pores can be observed on the grids of both PH and PHI scaffolds. Larger interconnected pores emerge in the PHI group. The differences of pore sizes can be attributed to the addition of DMSO, which is used to dissolve icariin in the PHI group. Interestingly, these pores appeared to be enveloped by the decorated SIS in the PHIS group. EDS analyses further reveals the elemental composition of the scaffolds, identifying the C, O, Ca, and P as predominant (Fig. 2(C)). Notably, the PHIS group possesses the highest ratios of Ca (4.6%,) and P (2.0%), which evenly distributes on the sample surface, indicative of an enhanced mineral-like content that is essential for bone tissue engineering (Fig. S1, ESI†).

The FTIR analysis provides further insights into the chemical functional groups on sample surface. All samples exhibit distinct absorption bands at 1748, 1452, 1178, and 1083 cm^{-1}, corresponding to the vibrational modes of C═O, C–H, symmetrical stretching vibration and asymmetrical stretching vibration of C–O–C, respectively. In contrast, the SIS displays characteristic peaks at 3350, 1600, 1430, 1083 cm^{-1}, associated with the –OH, N–H, C–H bonds, and asymmetrical stretching vibration of C–O–C, respectively. Noteworthily, the PHIS which combines all components, shows additional absorption bonds at 3300, 1636, and 1543 cm^{-1}, representative of –OH, C═C, and $-NO_2$ bonds, respectively (Fig. 3(A)). These results indicate successful

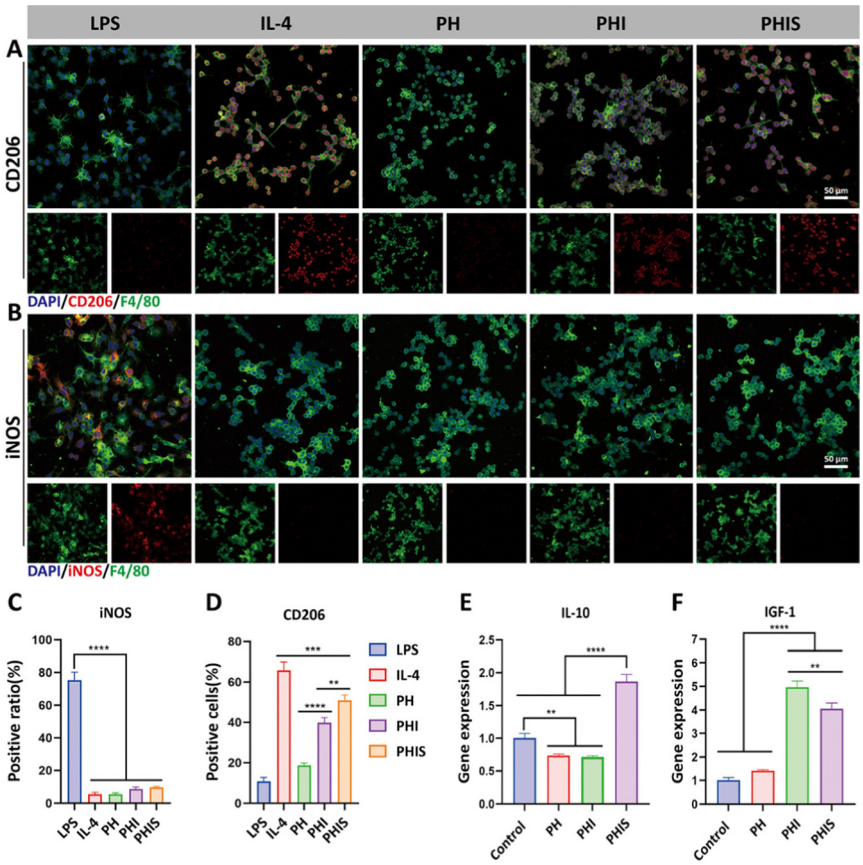

Fig. 5 Inflammatory response of macrophage on the 3D-printed scaffold *in vitro*. (A)–(D) Immunofluorescence and statistics of CD206 (A), (D) and iNOS (B), (C); (E) and (F) Relative mRNA expressions of anti-inflammatory genes. *$p < 0.05$, **$p < 0.01$, ***$p < 0.001$, ****$p < 0.0001$.

integration of SIS onto the surface of 3D-pined scaffold by the crosslinking action of EDC/NHS.

Furthermore, the XRD spectra of all 3D-printed scaffolds display the characteristic peaks of crystalline HAP at (002), (211), (112), (300), (310), (222), (213), and (004) planes, corresponding to the typical diffraction pattern of hexagonal HAP (JCPDS-no. 09-0432) (Fig. 3(B)). No significant differences of XRD peaks are found among those 3D-printed scaffolds, indicating that pure and well-crystallized hydroxyapatite particles are successfully incorporated into the 3D-printed scaffolds.[38] The TG-DSC analysis show the effect of temperature ranging from 30–1000 °C on the thermal stability of the 3D-printed scaffolds, and no differences exist among three 3D-printed groups (Fig. 3(C)). The weight loss from 300 °C to 375 °C can be attributed to the decomposition and combustion of organic components of PLGA, while only slight changes are observed from 375 °C to 1000 °C, which indicates the high stability of the synthesized HAP. Mechanical tests are performed to assess the mechanical properties of those 3D-printed scaffolds. As shown in Fig. 3(D), the PH group exhibits the highest mechanical behavior, while the PHI group presents the lowest mechanical behavior. This phenomenon can be attributed to the lyophilization of solvent DMSO used in the PHI group, which forms larger interconnected pores on the grids and consequently reduces the mechanical properties of scaffold to some extent. Interestingly, the mechanical behavior is significantly elevated after coating and crosslinking with SIS.

The release profiles of calcium and phosphorus are detected by ICP-OES. The results indicate that the highest release profile of both calcium and phosphorus are observed in the PHI group, whereas the lowest release profiles are detected in the PH group (Fig. 3(E) and (F)). The degradation assay presents a similar trend (Fig. S2, ESI†). Besides, the release of icariin from the 3D-printed scaffolds is analyzed by HPLC, where lower release

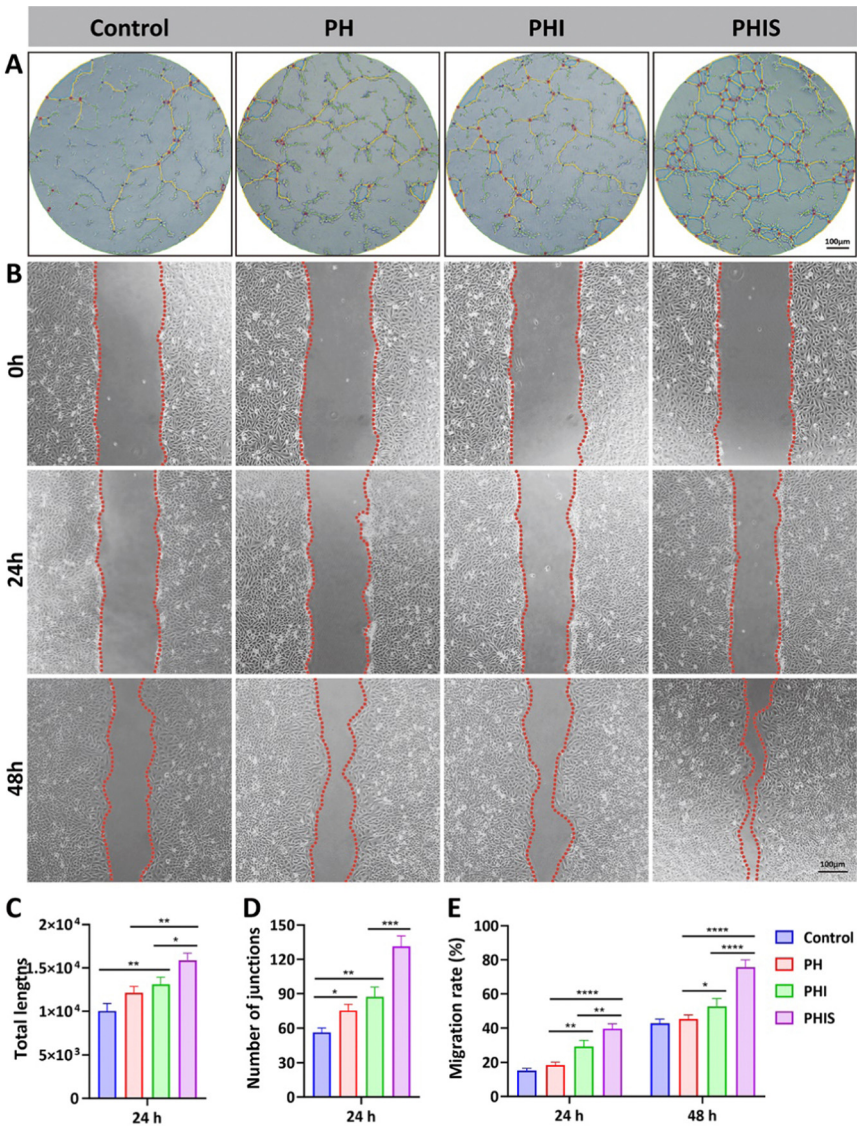

Fig. 6 Evaluation of angiogenic effect of the 3D-printed scaffolds *in vitro*. Tube formation assay (A), statistical analyses of total length (C) and number of junctions (D); scratch assay (B) and statistics of migration rate (E). *$p < 0.05$, **$p < 0.01$, ***$p < 0.001$, ****$p < 0.0001$.

profile is observed in the PHIS group compared to the PHI group (Fig. 4(A)). Therefore, the decoration of SIS on the 3D-printed PLGA/HA/ICA scaffold not only enhances the mechanical and degradative performance, but also prolongs the icariin release of fabricated scaffold.

3.2 Biocompatibility of the 3D-printed scaffolds

Biocompatibility is a crucial factor in assessing the safety of biomaterials for implantation.[15] In this study, the biocompatibility of 3D-printed scaffolds was evaluated through the CCK-8 assay and live/dead staining employing calcein-AM and PI. The CCK-8 results indicate a significant enhancement in proliferation of BMSCs cultured on all 3D-printed scaffolds, with the PHIS group demonstrating the highest proliferation rate from the second day onwards ($p < 0.05$, compared to the control, PH, and PHIS groups) (Fig. 4(B)). The increase in cell proliferation within the 3D-printed groups can be ascribed to the three-dimensional structure that facilitates cell growth compared to the two-dimensional surface in the control group.

The live/dead staining revealed strong attachment of BMSCs on all scaffold types. Nevertheless, the PH group displays a slightly higher incidence of cell mortality, as indicated by PI staining (Fig. 4(C)). It is also observed that the PHI group show higher cell densities than the PH group. Furthermore, the best cytocompatibility is provided by the PHIS group with the least dead cells being detected, which suggests the positive effect of SIS on cell growth and survival in accordance with our previous studies.[31–33]

3.3 Inflammatory response of macrophages

The innate immune response plays a pivotal role in regeneration of bone defects. In diabetic conditions, macrophages tend to shift towards inflammatory M1 phenotype, resulting in the release of numerous inflammatory cytokines, while the presence of pro-healing M2 macrophages is significantly reduced.[11,39] This imbalance in the immune environment under diabetic conditions hampers the natural process of bone defect regeneration.[12]

In this study, the immunomodulatory ability of 3D-printed scaffolds is assessed using RAW264.7 cells, which are cultured in extracts derived from the scaffolds for two days. The immunofluorescence staining of CD206, which is a marker indicative of the anti-inflammatory M2 phenotype, reveals a significant predominance of M2 macrophage in the PHS group than both PH and PHI groups ($p < 0.05$) (Fig. 5(A) and (D)). Notably, PHI group also shows an elevated expression of CD206 compared to the PH group, suggesting that addition of icariin to the scaffolds contributed to macrophage polarization towards the M2 phenotype. This aligns with existing literature which has documented the ability of icariin to induce M2 macrophage polarization, though not to the extent observed in the PHIS group.[40] Furthermore, the expression level of iNOS, a marker for the pro-inflammatory M1 macrophage phenotype, remains below 12% across all the groups (Fig. 5(B) and (C)), suggesting that none of the scaffolds induce a significant inflammatory response.

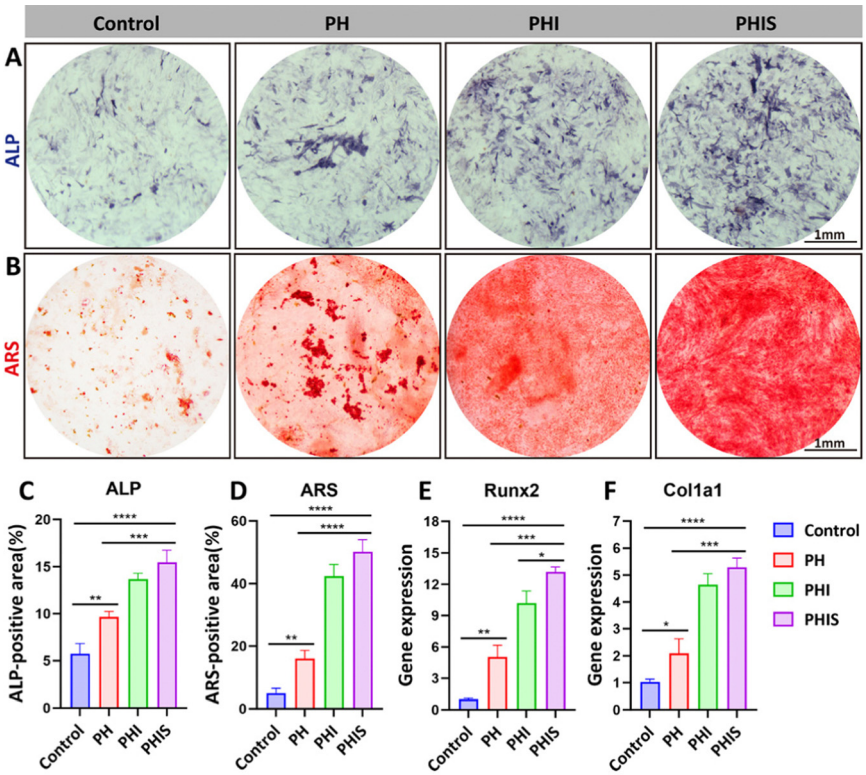

Fig. 7 Evaluation of osteogenic effect of the 3D-printed scaffolds *in vitro*. ALP staining (A) and statistics (C); ARS staining (B) and statistics (D); (E) and (F) relative mRNA expressions of osteogenic genes. *$p < 0.05$, **$p < 0.01$, ***$p < 0.001$, ****$p < 0.0001$.

The immunomodulatory potential of the 3D-printed scaffolds is further reinforced by the qPCR analysis, which shows a marked elevation in the mRNA levels of IL-10 and IGF-1 within the PHIS group compared to both the control and PH groups ($p < 0.05$) (Fig. 5(E) and (F)). IL-10 and IGF-1 are well recognized as anti-inflammatory cytokines.[41–43] The presence of M2 macrophages and the elevated expression of cytokines like IL-10 and IGF-1 in the PHIS group significantly mitigate the chronic inflammatory milieu associated with diabetes, thereby creating a more conductive environment for bone defect regeneration in diabetic individuals.

3.4 *In vitro* angiogenic behavior

Angiogenesis is another critical process in bone defect regeneration, particularly in diabetic conditions.[44] Diabetic pathology is characterized by impaired angiogenesis, highlighting the necessity for materials to possess angiogenic induction capabilities.[7,9] Our previous study has shown that composite SIS hydrogel exhibits significant immunomodulatory and angiogenic properties, capable of inducing macrophage polarization from M1 to M2 and potentially activating the JAK-STAT signal pathways.[32] In addition, SIS has also been proved to promote tube formation and migration of HUVECs, due to the impregnated cytokines like VEGF and bFGF within its dECM.[30]

In this study, we explore the use of SIS hydrogel as a coating for 3D-printed scaffolds, which are then crosslinked with EDC/NHS to ensure stability and integration. The efficacy of these modified scaffolds in promoting angiogenesis are evaluated through tube formation assays and HUVEC migration tests. The PHIS group outperforms the control, PH, and PHI groups in both the total length of the formed tubes and the number of junctions ($p < 0.05$) (Fig. 6(A), (C) and (D)). Moreover, HUVECs migration assays indicate that cells migrate more rapidly in PHIS group at both 24 and 48 h intervals compared to the other three groups ($p < 0.05$) (Fig. 6(B) and (E)). The angiogenic mRNA expressions are also tested, where the PHIS group detects the highest expression. Interestingly, the PHI group also shows some advantages in elevating the mRNA expression of angiogenesis-associated genes (Fig. S3, ESI†).

Those findings demonstrate the enhanced angiogenic properties of the 3D-printed scaffolds when coated with SIS, even after crosslinking with EDC/NHS. The preserved bioactivity of SIS within this composite material meets the requirement for angiogenic induction in diabetic bone regeneration, addressing

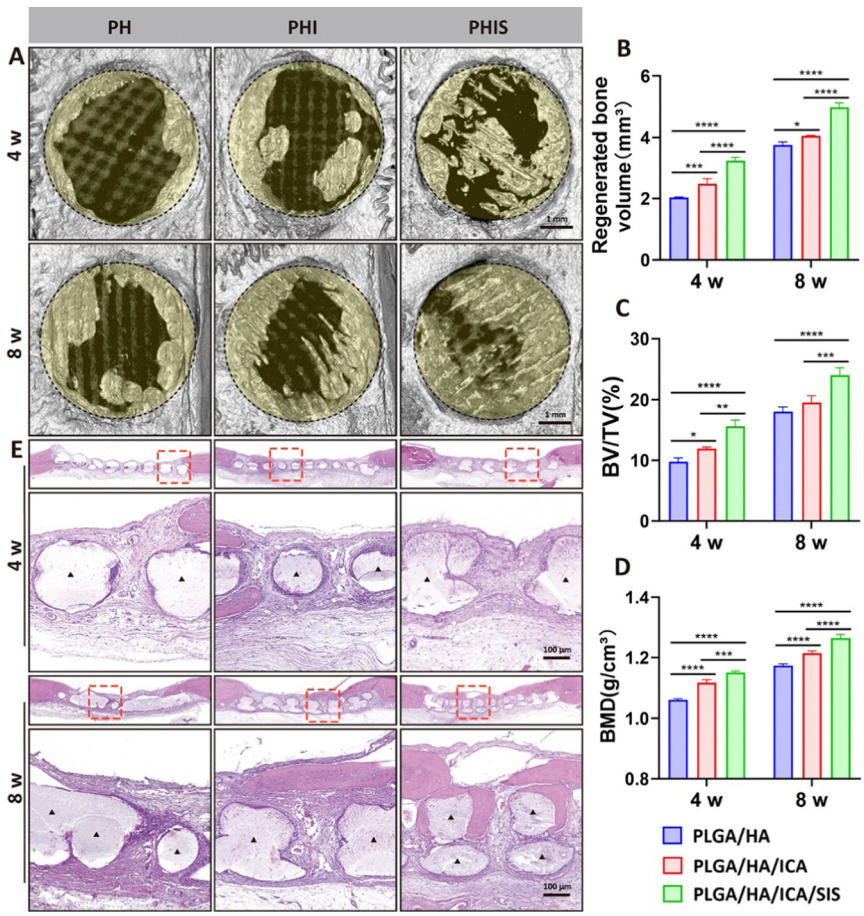

Fig. 8 Bone regeneration efficacy of the 3D-printed scaffolds implanted in diabetic rats *in vivo*. (A) Micro-CT scans; (B)–(D) statistical histograms of regenerated bone volume (B), BV/TV (C), and BMD (D); (E) H&E staining. BV, bone volume; TV, total volume; BMD, bone mineral density. ▲ denotes the 3D-printed scaffolds. *$p < 0.05$, **$p < 0.01$, ***$p < 0.001$, ****$p < 0.0001$.

the challenge posed by the diminished microvascular network in diabetic conditions.

3.5 *In vitro* osteogenic behavior

The osteogenic potential of 3D-printed scaffolds is crucial for bone regeneration materials.[17] The ALP staining, a marker of early osteogenic differentiation, shows that the PHIS group manifests the most significant expression among all groups (Fig. 7(A) and (C)), with an average positive staining area of 15.46 ± 1.29% ($p < 0.05$, *vs.* control and PH groups). The ARS staining presents similar trends, where the PHIS group demonstrates the highest mineralization level (Fig. 7(B) and (D)), with an average positive area of 50.17 ± 3.79% ($p < 0.05$, *vs.* control and PH groups). The qPCR analysis further corroborates these results, showing significant upregulation of osteogenic genes in the PHIS groups (Fig. 7(E) and (F)). Specifically, the expression levels of *Runx-2* and *Col1a1*, crucial genes involved in osteogenesis, are markedly elevated in the PHIS group ($p < 0.05$, *vs.* control and PH groups for *Col1a1*; $p < 0.05$, *vs.* control, PH, and PHI groups for *Runx-2*). The superior osteogenic induction capability observed in the PHIS group can be attributed to the synergistic effects of icariin and SIS incorporation within the scaffolds. Additionally, the PHIS group possesses higher concentrations of Ca and P (4.6% for Ca, 2.0% for P), both of which are recognized as conductive elements for osteogenesis.[45–47]

3.6 Micro-CT analysis

The *in vivo* osteogenic behaviors of these 3D-printed scaffolds are evaluated after their implantation into the skulls of diabetic rats. After 4 weeks implantation, Micro-CT scans reveal that the PHIS group results in the highest regenerated bone volume, bone volume/total volume (BV/TV), and bone mineral density (BMD) ($p < 0.05$, *vs.* PH and PHI groups) (Fig. 8(A)–(D)). Additionally, the PHI group also shows enhanced bone regeneration metrics compared to the PH group, with significant increases in regenerated bone volume, BV/TV, and BMD ($p < 0.05$). After 8 weeks implantation, the PHIS group continued to dominate in all measured parameters of bone regeneration. Although the PHI group maintained higher regenerated bone volume and BMD compared to the PH group, no significant difference in BV/TV is observed between them. The observed enhancement in osteogenic activity, particularly in scaffolds

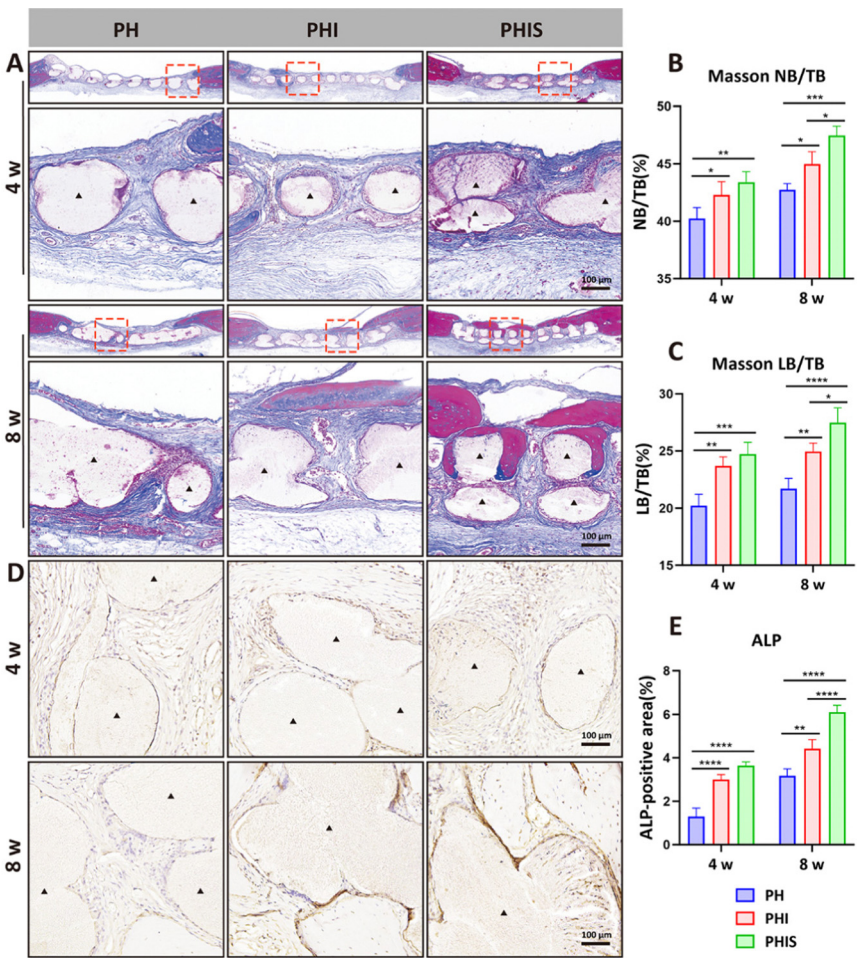

Fig. 9 Osteogenic evaluation of the 3D-printed scaffolds *in vivo*. (A) Masson's trichrome staining; (B) and (C) statistical histograms of (B) NB/TB and (C) LB/TB based on Masson's trichrome staining; (D) and (E) ALP staining (D) and statistical histogram (E). NB, new bone; LB, lamellar bone; TB, total bone. ▲ denotes the 3D-printed scaffolds. *$p < 0.05$, **$p < 0.01$, ***$p < 0.001$, ****$p < 0.0001$.

incorporating icariin (PHI and PHIS groups), corroborates previous research findings that icariin is a potent agent in stimulating both angiogenesis and bone regeneration.[48]

3.7 HE and Masson's trichrome staining

To further evaluate the quality of the bone regeneration in the diabetic rat skulls, histological examinations are conducted using HE and Masson's trichrome staining. Four weeks post-implantation, staining results reveal significant migration of cells towards vicinity of the PHI and PHIS group scaffolds, with notable cellular infiltration observed within the PHIS group. In contrast, the PH group displayed minimal cellular infiltration (Fig. 8(E) and 9(A)). The evaluation of the regenerated bone is quantified by analyzing the new bone area to total bone area ratio (NB/TB) and lamellar bone area to total bone area ratio (LB/TB). Consistent with the micro-CT findings, the PHI and PHIS groups exhibit higher NB/TB and LB/TB ratios ($p < 0.05$, *vs.* PH group) (Fig. 9(B) and (C)), indicating more collagen fibers are deposited within the diabetic bone defect area, although no statistical differences are observed between them. 8 weeks post-implantation, both NB/TB and LB/TB ratios increase significantly in all groups (Fig. 9(B) and (C)), with the PHIS group maintaining the highest levels of both metrics ($p < 0.05$, *vs.* PH and PHI groups). Notably, the vicinity of the PHIS scaffolds displayed pronounced calcified lamellar bone structures, a feature less prominent in the PH and PHI groups (Fig. 9(A)). These findings corroborate the beneficial effects of integrating of icariin and SIS into the 3D-printed scaffolds, enhancing their capacity to foster new bone formation and calcification in diabetic conditions.

3.8 Immunohistochemical and immunofluorescent analysis

Immunohistochemistry of ALP, a hallmark marker for early-stage osteogenesis,[49] is employed to assess osteogenesis within the scaffold-implanted regions. ALP staining at 4 weeks post-implantation reveals markedly higher expression levels in the PHI and PHIS groups compared to the PH group. Specifically, ALP expression is quantified at 3.0 ± 0.23% in the PHI group

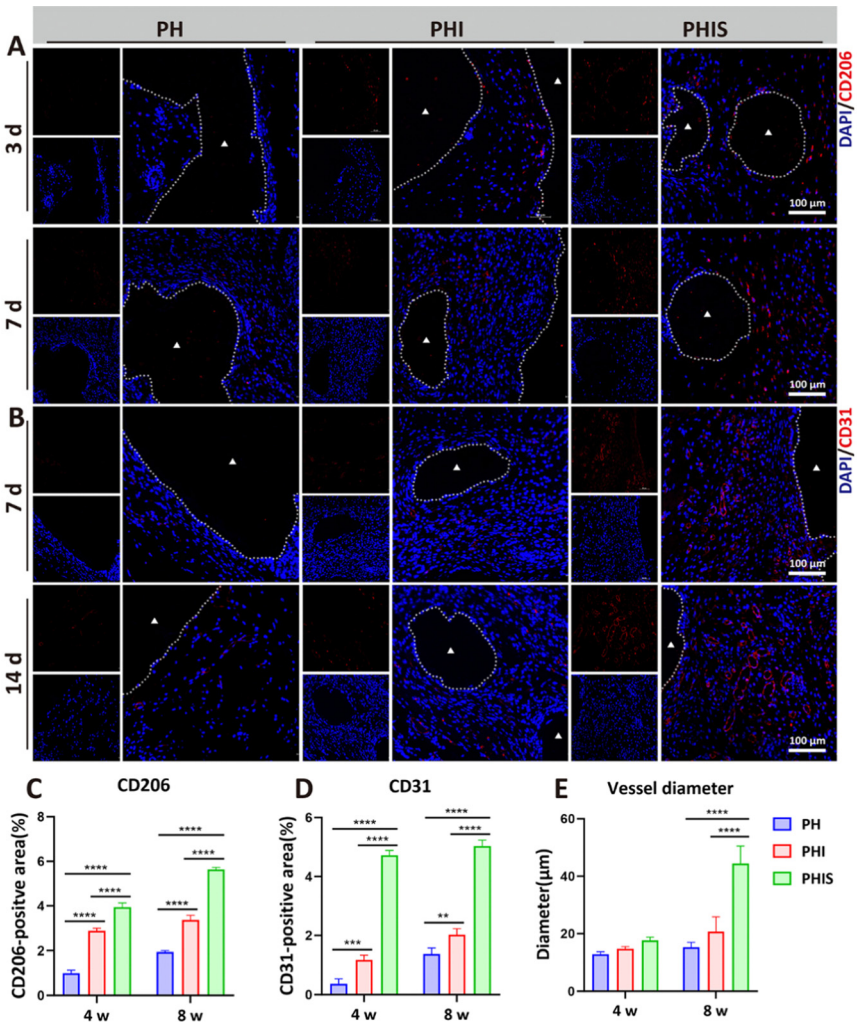

Fig. 10 The immunomodulatory and angiogenic capacities of the 3D-printed scaffolds *in vivo*. CD206 immunofluorescence (A) and statistical histogram (C); CD31 immunofluorescence (B) and statistical histogram (D); (E) Diameter of newly formed blood vessel based on CD31 staining. ▲ denotes the 3D-printed scaffolds. **p < 0.01, ***p < 0.001, ****p < 0.0001.

and 3.63 ± 0.18% in the PHIS group. By the 8 weeks post-implantation, these levels have increased to 4.43 ± 0.42% in the PHI group and 6.11 ± 0.32% in the PHIS group, showing a significant progression in the osteogenic expression over time ($p < 0.05$, *vs.* PH group) (Fig. 9(D) and (E)). Notably, the difference in ALP expression between the PHI and PHIS groups is not statistically significant at 4 weeks (3.0 ± 0.23% *vs.* 3.63 ± 0.18%, $p > 0.05$). However, by the 8-week point, a significant divergence emerged, with the PHIS group displaying substantially higher ALP levels compared to the PHI group (4.43 ± 0.42% *vs.* 6.11 ± 0.32%, $p < 0.05$), aligning with the trends that observed in the results of micro-CT scans and Masson's trichrome staining. These findings suggest a similar pattern of bone regeneration in the PHI and PHIS groups. The enhanced bone formation can be ascribed to the addition of potent osteogenic properties of icariin. The peak in ALP expression and overall efficacy in bone regeneration within the diabetic rat skulls, especially noted in the PHIS group, prompts a deeper investigation into the underlying mechanisms, which will be explored further.

As previously described, the innate immune response of host plays a crucial role in bone regeneration, particularly in the context of diabetes.[12] In diabetic conditions, the M1 macrophages secrete multiple pro-inflammatory cytokines that interfere with the normal healing processes.[11] Additionally, diabetes is characterized by the loss of small blood capillaries, further impeding the timely regeneration of bone tissue.[6,9] Given these challenges, innovative materials that possess immunoregulatory properties to facilitate diabetic bone regeneration is highly desirable. Our *in vitro* experiments have revealed that the 3D-printed PHIS scaffold exhibits promising immunoregulatory and angiogenic properties.

To elucidate the *in vivo* immunoregulatory and angiogenic potentials of the 3D-printed scaffolds, their implantation effects were studied in detail. The expression of CD206 progressively increase from 3 to 7 days, with the PHIS group exhibits the highest levels at both 3 (3.94 ± 0.19%) and 7 days (5.64 ± 0.1%) compared to PH and PHI groups ($p < 0.05$) (Fig. 10(A) and (C)). The PHI group also shows increased CD206 expression compared to the PH group (2.89 ± 0.11% at day 3 and 3.37 ± 0.21% at day 7; $p < 0.05$), although not as pronounced as the PHIS group. These enhancement in CD206 expression can be associated with the anti-inflammatory effects of icariin, which has been reported to mitigate inflammation in senescent macrophages through autophagy activation.[36]

The expression of CD31,[50] a typical biomarker of blood vessels, around the implanted scaffolds reveals an increasing trend from day 7 to day 14 (Fig. 10(B)). Statistical analysis of the CD31-positive area reveals that the PHIS group displays significantly larger positive areas than the PH and PHI groups at both day 3 (4.72 ± 0.17%) and day 7 (5.03 ± 0.20%) (Fig. 10(D)). Remarkably, the diameter of newly formed blood vessels within the PHIS group exhibited substantial growth, expanding from 17.62 ± 1.16 μm at day 7 to 44.37 ± 6.09 μm at day 14 ($p < 0.05$, *vs.* the PH and PHI groups). In contrast, the PH and PHI groups display blood vessel diameters below 25 μm at all observed time points (Fig. 10(E)).

4. Conclusion

Diabetes presents a significant challenge to bone defect healing due to its characteristic inflammatory microenvironment and diminished small blood vessels. In this study, a novel 3D-printed scaffold composed of PLGA, HA, and icariin, and further functionalized with SIS (PHIS), was developed to address these challenges. Its immunomodulatory and angiogenic capacities are tested *in vitro* and *in vivo*. Our results indicated that the SIS coating enhances the bioactivity of the scaffold by encouraging the polarization of macrophages towards an M2 phenotype, which thus ameliorated the inflammatory conditions characteristic of diabetic bone defects and fostered a more favorable healing environment. Moreover, the scaffold also noted an excellent capacity to bolster the angiogenic potential of HUVECs, evidently through enhancing the migration and tube formation of the vascular cells. The combined immunomodulatory and angiogenic capabilities of the PHIS scaffold align well with the treatment demands of diabetic pathology, making it an effective tool for accelerating bone defect regeneration in diabetic patients.

Author contributions

Jie Tan: formal analysis, methodology, original draft writing. Zecai Chen: methodology, formal analysis, statistics, original draft writing. Zhen Xu: formal analysis, methodology. Yafang Huang: histology. Lei Qin: methodology. Yufeng Long: methodology. Jiayi Wu: methodology. Hantao Yang: methodology. Xuandu Chen: methodology. Weihong Yi: methodology, conception. Ruiqiang Hang: methodology, draft revision. Min Guan: methodology, draft revision. Huaiyu Wang: methodology, research supervision, draft revision. Ang Gao: methodology, research supervision, draft revision. Dazhi Yang: methodology, research supervision, draft revision.

Data availability

The data supporting this article have been included as part of the ESI.†

Conflicts of interest

The authors listed declare no conflict of interest.

Acknowledgements

This study has been jointly sponsored by National Key Research and Development Program of China (grant no. 2021YFB 3800800), Guangdong Basic and Applied Basic Research Foundation (grant no. 2022A1515010528, 2022A1515220036, 2023A1515220194, and 2024A1515012397), Shenzhen Science

and Technology Program (grant no. JSGG20210802153156021, JCYJ20210324101800002), Major Project of Nanshan Health Committee (grant no. NSZD2023036, NSZD2023009, NSZD2024019, and NS2024011), and Project of Nanshan People's Hospital (grant no. YN2022010).

References

1 J. Dong, H. Ding, Q. Wang and L. Wang, *Polymers*, 2024, **16**, 706.
2 T. Chen, Z. Wu, Q. Hou, Y. Mei, K. Yang, J. Xu and L. Wang, *Int. J. Nanomed.*, 2024, **19**, 2709–2732.
3 Z. Li, M. Yue and Y. Zhou, *Stem Cells Transl. Med.*, 2024, **13**, 243–254.
4 A. V. A. Mariadoss, A. S. Sivakumar, C. H. Lee and S. J. Kim, *Biomed. Pharmacother.*, 2022, **151**, 113134.
5 K. Hygum, J. Starup-Linde, T. Harsløf, P. Vestergaard and B. L. Langdahl, *Eur. J. Endocrinol.*, 2017, **176**, R137–r157.
6 S. Khosla, P. Samakkarnthai, D. G. Monroe and J. N. Farr, *Nat. Rev. Endocrinol.*, 2021, **17**, 685–697.
7 A. Sheu, J. R. Greenfield, C. P. White and J. R. Center, *Trends Endocrinol. Metab.*, 2023, **34**, 34–48.
8 G. P. Fadini, F. Ferraro, F. Quaini, T. Asahara and P. Madeddu, *Stem Cells Transl. Med.*, 2014, **3**, 949–957.
9 T. Le, A. Salas Sanchez, D. Nashawi, S. Kulkarni and R. D. Prisby, *Curr. Osteoporos. Rep.*, 2024, **22**, 11–27.
10 L. Tong, A. J. van Wijnen, H. Wang and D. Chen, *Innov. Life*, 2024, **2**, 100078.
11 N. Sheng, F. Xing, Q.-Y. Zhang, J. Tan, R. Nie, K. Huang, H.-X. Li, Y.-L. Jiang, B. Tan, Z. Xiang and H.-Q. Xie, *Chem. Eng. J.*, 2024, **480**, 147985.
12 N. Sheng, F. Xing, J. Wang, Q.-Y. Zhang, R. Nie, J. Li-Ling, X. Duan and H.-Q. Xie, *Mater. Today Bio*, 2023, **23**, 100835.
13 F. Zhao, A. Gao, Q. Liao, Y. Li, I. Ullah, Y. Zhao, X. Ren, L. Tong, X. Li, Y. Zheng, P. K. Chu and H. Wang, *Adv. Funct. Mater.*, 2024, **34**, 2311812.
14 Y. Wu, H. Wang and P. K. Chu, *Innov. Life*, 2023, **1**, 100027.
15 W. Huiwen, L. Shuai, X. Jia, D. Shihao, W. Kun, Y. Runhuai, Q. Haisheng and L. Jun, *J. Biol. Eng.*, 2024, **18**, 22.
16 A. A. Menarbazari, A. Mansoori-Kermani, S. Mashayekhan and A. Soleiymani, *Int. J. Biol. Macromol.*, 2024, **265**, 130827.
17 A. Kara, T. Distler, C. Polley, D. Schneidereit, H. Seitz, O. Friedrich, F. Tihminlioglu and A. R. Boccaccini, *Mater. Today Bio*, 2022, **15**, 100309.
18 Z. Jing, W. Yuan, J. Wang, R. Ni, Y. Qin, Z. Mao, F. Wei, C. Song, Y. Zheng, H. Cai and Z. Liu, *Bioact. Mater.*, 2024, **33**, 223–241.
19 M. Lian, Z. Qiao, S. Qiao, X. Zhang, J. Lin, R. Xu, N. Zhu, T. Tang, Z. Huang, W. Jiang, J. Shi, Y. Hao, H. Lai and K. Dai, *ACS Nano*, 2024, **18**, 7504–7520.
20 D. Fernández-Villa, M. R. Aguilar and L. Rojo, *J. Mater. Chem. B*, 2024, **12**, 7153–7170.
21 Y. Huang, Y. Xu, Z. Huang, J. Mao, Y. Hui, M. Rui, X. Jiang, J. Wu, Z. Ding, Y. Feng, Y. Gu and L. Chen, *J. Mater. Chem. B*, 2024, **12**, 7367–7383.
22 X. Yang, L. Wu, C. Li, S. Li, W. Hou, Y. Hao, Y. Lu and L. Li, *ACS Appl. Mater. Interfaces*, 2024, **16**, 3171–3186.
23 Q. Li, Q. Li, S. Lu and D. Pan, *Nanomaterials*, 2023, **13**, 3113.
24 Z. Du, F. Qiao, L. Tong, W. Zhang, X. Mou, X. Zhao, M. F. Maitz, H. Wang, N. Huang and Z. Yang, *Innovation*, 2024, **5**, 100671.
25 E. Pesaranhajiabbas, M. Misra and A. K. Mohanty, *Int. J. Biol. Macromol.*, 2023, **253**, 126231.
26 S. Murab, S. Herold, T. Hawk, A. Snyder, E. Espinal and P. Whitlock, *J. Mater. Chem. B*, 2023, **11**, 7250–7279.
27 J. E. Song, D. H. Lee, G. Khang and S. J. Yoon, *Int. J. Biol. Macromol.*, 2023, **229**, 486–495.
28 Y. Dou, J. Huang, X. Xia, J. Wei, Q. Zou, Y. Zuo, J. Li and Y. Li, *J. Mater. Chem. B*, 2021, **9**, 4488–4501.
29 W. He, C. Li, S. Zhao, Z. Li, J. Wu, J. Li, H. Zhou, Y. Yang, Y. Xu and H. Xia, *Bioact. Mater.*, 2024, **34**, 338–353.
30 W. Wang, X. Zhang, N. N. Chao, T. W. Qin, W. Ding, Y. Zhang, J. W. Sang and J. C. Luo, *Acta Biomater.*, 2016, **29**, 135–148.
31 R. Nie, Q.-Y. Zhang, J. Tan, Z.-Y. Feng, K. Huang, N. Sheng, Y.-L. Jiang, Y.-T. Song, C.-Y. Zou, L.-M. Zhao, H.-X. Li, R. Wang, X.-L. Zhou, J.-J. Hu, C.-Y. Wu, J. Li-Ling and H.-Q. Xie, *Composites, Part B*, 2023, **267**, 111005.
32 J. Tan, Q.-Y. Zhang, Y.-T. Song, K. Huang, Y.-L. Jiang, J. Chen, R. Wang, C.-Y. Zou, Q.-J. Li, B.-Q. Qin, N. Sheng, R. Nie, Z.-Y. Feng, D.-Z. Yang, W.-H. Yi and H.-Q. Xie, *Composites, Part B*, 2022, **243**, 110149.
33 Q.-Y. Zhang, J. Tan, R. Nie, Y.-T. Song, X.-L. Zhou, Z.-Y. Feng, K. Huang, C.-Y. Zou, Q.-J. Yuan, L.-M. Zhao, X.-Z. Zhang, Y.-L. Jiang, L.-M. Liu, J. Li-Ling and H.-Q. Xie, *Composites, Part B*, 2023, **254**, 110550.
34 Y. Xu, Y. Li, A. Gao, P. K. Chu and H. Wang, *Innov. Life*, 2023, **1**, 100015.
35 L. Zou, L. Hu, P. Pan, S. Tarafder, M. Du, Y. Geng, G. Xu, L. Chen, J. Chen and C. Lee, *Composites, Part B*, 2022, **232**, 109625.
36 L. Bai, Y. Liu, X. Zhang, P. Chen, R. Hang, Y. Xiao, J. Wang and C. Liu, *Biomaterials*, 2023, **297**, 122125.
37 C. Li, W. Zhang, Y. Nie, X. Du, C. Huang, L. Li, J. Long, X. Wang, W. Tong, L. Qin and Y. Lai, *Adv. Mater.*, 2023, e2308875, DOI: 10.1002/adma.202308875,.
38 N. Hashemi, Z. Vaezi, S. Masoumi, S. S. Mohammadi, R. Mahdavian, M. Sedghi, H. Redl, A. Banerjee, A. Weidinger and H. Naderi-Manesh, *Ceram. Int.*, 2022, **48**, 4200–4207.
39 Y. Wang, Q. Lin, H. Zhang, S. Wang, J. Cui, Y. Hu, J. Liu, M. Li, K. Zhang, F. Zhou, Y. Jing, Z. Geng and J. Su, *Bioact. Mater.*, 2023, **28**, 273–283.
40 Y. Y. Teng, M. L. Zou, S. Y. Liu, Y. Jia, K. W. Zhang, Z. D. Yuan, J. J. Wu, J. X. Ye, S. Yu, X. Li, X. J. Zhou and F. L. Yuan, *Front. Bioeng. Biotechnol.*, 2022, **10**, 902894.
41 C. Wang, T. Li, X. Zeng, L. Wu, M. Gao, N. Tong, P. Duan and J. Liu, *Dent. Mater.*, 2023, **39**, 418–429.
42 X. Cao, L. Duan, H. Hou, Y. Liu, S. Chen, S. Zhang, Y. Liu, C. Wang, X. Qi, N. Liu, Z. Han, D. Zhang, Z. C. Han, Z. Guo, Q. Zhao and Z. Li, *Theranostics*, 2020, **10**, 7697–7709.

43 S. Y. Chu, C. H. Chou, H. D. Huang, M. H. Yen, H. C. Hong, P. H. Chao, Y. H. Wang, P. Y. Chen, S. X. Nian, Y. R. Chen, L. Y. Liou, Y. C. Liu, H. M. Chen, F. M. Lin, Y. T. Chang, C. C. Chen and O. K. Lee, *Nat. Commun.*, 2019, **10**, 1524.
44 L. Liu, C. X. Zheng, N. Zhao, T. Zhu, C. B. Hu, N. Zhang, J. Chen, K. C. Zhang, S. Zhang, J. X. Liu, K. Zhang, H. Jing, B. D. Sui, Y. Jin and F. Jin, *Adv. Healthcare Mater.*, 2023, **12**, e2300019.
45 Y. Shi, W. Tao, W. Yang, L. Wang, Z. Qiu, X. Qu, J. Dang, J. He and H. Fan, *J. Nanobiotechnol.*, 2024, **22**, 47.
46 S. Vermeulen, K. Knoops, H. Duimel, M. Parvizifard, D. van Beurden, C. López-Iglesias, S. Giselbrecht, R. Truckenmüller, P. Habibović and Z. Tahmasebi Birgani, *Mater. Today Bio*, 2023, **23**, 100844.
47 Y. Zhou, Z. Hu, W. Jin, H. Wu, M. Zuo, C. Shao, Y. Lan, Y. Shi, R. Tang, Z. Chen, Z. Xie and J. Shi, *Adv. Healthcare Mater.*, 2023, **12**, e2201548.
48 S. Li, Y. Cui, H. Liu, Y. Tian, Y. Fan, G. Wang, J. Wang, D. Wu and Y. Wang, *Mater. Today Bio*, 2024, **24**, 100943.
49 Y. Wu, R. Liang, W. Chen, C. Wang and D. Xing, *Talanta*, 2024, **270**, 125622.
50 V. Crenn, J. Amiaud, A. Gomez-Brouchet, V. Potiron, F. Gouin, P. Rosset, L. L. Nail, L. Vidal, H. Bertin, R. Brion, G. Tran, F. Verrecchia, I. Corre and F. Redini, *Am. J. Cancer Res.*, 2022, **12**, 1843–1854.